ANL/MSD/CP--88946
CONF-960202--7

IN SITU HVEM STUDIES OF PHASE TRANSFORMATION IN Zr ALLOYS AND COMPOUNDS UNDER IRRADIATION*

Arthur T. Motta[1], Joseph A. Faldowski[1], Lawrence M. Howe[2] and Paul R. Okamoto[3]

[1]Dept. of Nuc. Eng., Pennsylvania State University
University Park, PA 16802

[2]AECL Research Reactor Materials Branch, Chalk River Laboratories,
Ontario, Canada, K0J 1J0

[3]Materials Science Division, Argonne National Laboratory,
Argonne, IL 60439

January 1996

Invited Paper presented at the 11th International Symposium on Zirconium in the Nuclear Industry, 2/4-8/96, Anaheim, California. To be published as a book chapter of ASTM STP - 1996.

*Work supported by the U. S. Department of Energy, BES-Materials Sciences, under Contract W-31-109-Eng-38.

Abstract

The High Voltage Electron Microscope (HVEM)/Tandem facility at Argonne National Laboratory has been used to conduct detailed studies of the phase stability and microstructural evolution in zirconium alloys and compounds under ion and electron irradiation. Detailed kinetic studies of the crystalline-to-amorphous transformation of the intermetallic compounds $Zr_3(Fe_{1-x},Ni_x)$, $Zr(Fe_{1-x},Cr_x)_2$, Zr_3Fe, and $Zr_{1.5}\,Nb_{1.5}\,Fe$, both as second phase precipitates and in bulk form, have been performed using the in-situ capabilities of the Argonne facility, under a variety of irradiation conditions (temperature, dose rate). Results include a verification of a dose rate effect on amorphization and the influence of material variables (stoichiometry x, presence of stacking faults, crystal structure) on the critical temperature and on the critical dose for amorphization.

Studies were also conducted of the microstructural evolution under irradiation of specially tailored binary and ternary model alloys. The stability of the ω-phase in Zr-20%Nb under electron and Ar ion irradiation was investigated as well as the β-phase precipitation in Zr-2.5%Nb under Ar ion irradiation. The ensemble of these results is discussed in terms of theoretical models of amorphization and of irradiation-altered solubility.

Introduction

Various types of zirconium alloys have been employed during the past decades for cladding, tubing and structural materials in nuclear power reactor fuel elements. Among such alloys are Zircaloy-2 used in BWR, Zircaloy-4 used in PWR, the Canadian Zr-2.5%Nb used in Candu pressure tubes and calandria tubes, the Zr-1%Nb alloy used in VVER and RBMK reactors and other newer alloys such as ZIRLO. The alloying additions and optimized fabrication microstructures given by specified thermomechanical treatments give those alloys excellent resistance to high temperature corrosion, very good resistance to in-reactor deformation and good mechanical strength. These properties, combined with zirconium's low thermal neutron absorption cross section, has allowed for

superior performance of fuel cladding under the harsh conditions found in the cores of nuclear power reactors.

A great deal of knowledge has been accumulated during the last decades on in-reactor behavior of zirconium alloys [1-3]. Fabrication and irradiation procedures have been tightened and made more reproducible so that during normal operation there is a reasonable expectation of near zero cladding failures [4]. Most of this experience, however, is based on the operation up to 30 Gwd/ton (3 years in-reactor), with a fuel cycle of around one year and well-defined reactor temperature and water chemistry. Any major deviation in this combination of operational parameters puts the cladding in uncharted territory and makes its behavior less predictable. This is specially true for high fluence components such as pressure tubes in CANDU reactors, and high burnup cladding in LWR. At 30 GWd/ton the microstructure of the zirconium alloy components is still evolving [3], so that a breakaway regime could have its onset at 45 or 60 GWd/ton. In general it simply is not possible to have an experimental database that will cover all of the possible combinations of temperature, flux, flux spectrum, fluence, temperature, material composition, microstructure and water chemistry. The only hope of extending the existing database beyond its current limits is by understanding the mechanisms of radiation damage and microstructural evolution, and developing mechanistic models that can be applied in a more general sense.

In that regard, the use of charged-particle irradiation under controlled conditions for the study of mechanisms of irradiation damage has several benefits [5]. The higher dose rates afforded by charged particle (electron and ion) irradiation allow us to reach damage levels in displacements per atom (dpa) comparable to those obtained in neutron irradiation in much less time. We also have greater control of experimental parameters such as temperature and dose rate under charged particle irradiation than under neutron irradiation. It should be emphasized that charged particle irradiation should not be seen as a "simulation" of neutron irradiation per se, but as a different irradiation altogether. This is not a drawback, but a positive aspect of these irradiations, since they allow us to

explore different areas of phase space than it is possible with neutron irradiation. For example, it is possible to study the influence that displacement cascades have on a given process by irradiating the material with electrons since in contrast with neutrons they produce damage not in cascades but in isolated Frenkel pairs. It is necessary however, to couple the experiments with theoretical understanding of the processes, in order to draw any significant conclusions on operating mechanisms.

Among the possible means of irradiation with charged particles, a particularly useful one is the use of in-situ irradiation with high energy electrons and ions in an electron microscope. This means of irradiation has the additional advantage of allowing the detailed and systematic study of irradiation kinetics. This paper reports on such a study, conducted at the three institutions involved in collaboration with the goal of understanding the mechanisms and kinetics of phase transformations under electron and ion irradiation. We focus on the crystalline-to-amorphous transformation (amorphization) in Zr-based intermetallic compounds, the stability of ω-phase precipitates in Zr-Nb alloys and on the destabilization of Zr-Nb solid solutions with respect to β-phase precipitation.

Intermetallic precipitates in zirconium alloys have been extensively studied. The precipitates normally found in Zircaloys are of the type $Zr(Cr,Fe)_2$ (with a fcc C14 or hcp C15 structure) and $Zr_2(Ni,Fe)$ (bct C16 structure [6]. Zr_3Fe (orthorombic) based precipitates have been observed in alloys containing excess Fe [7] or after annealing of neutron-irradiated material [8]. The Fe/Cr and Fe/Ni ratios in Zircaloys can affect the alloy microstructure and behavior. We studied here the influence of internal stoichiometry in the pseudo-binary compound on amorphization. After reporting our results, we place them in the context of other experimental results and establish some guidelines for theoretical modeling.

All of these issues could have impact on cladding behavior. The amorphization of precipitates in Zircaloy has been linked to faster precipitate dissolution, with consequent changes to the alloy microchemistry which impact on atomic transport properties [44] and corrosion resistance [45]. In the

same way the irradiation induced β-phase precipitation in Zr-Nb alloys has been linked to improved corrosion resistance [46].

Experimental Methods

For the amorphization studies, model alloys were prepared at AECL, Chalk River Laboratory and The Pennsylvania State University by arc melting from pure components (Zr 99.8%, Cr 99.99%, Fe 99.98%, Ni 99.98%, Nb 99.9%) followed by appropriate heat treatment as described in [9]. Samples suitable for examination by Transmission Electron Microscopy (TEM) were prepared by mechanical grinding, and punching or spark cutting, followed by electropolishing with a 10% perchloric acid solution in methanol. The alloys prepared were Zr_3Fe, $Zr_3(Fe_{0.9}, Ni_{0.1})$, $Zr_3(Fe_{0.5},Ni_{0.5})$, $ZrCr_2$, $ZrFe_2$, and $Zr_{1.5}\ Nb_{1.5}\ Fe$.

The other alloys were prepared as follows: Zr-20%Nb plate material was annealed at 1123 K for 3 h, cooled to room temperature and then annealed at 673 K for 24 h to form an even dispersion of the omega phase. For the β-precipitation study, samples of Zr-2.5%Nb pressure tube material were annealed for 1 h at 970 K. Finally, the Zr-1%Nb alloy was made by arc melting. Slices of the alloy were annealed for 2 hours at 1223 K, then 17.7h at 1023 K, followed by vacuum quenching from 848 K. Following the heat treatment, TEM samples were prepared by a similar electropolishing method, as above.

The heat treatment and fabrication process resulted in three types of alloys:

a) $Zr_3(Fe_{1-x},Ni_x)$: This alloy was formed with the structure of the orthorombic Zr_3Fe phase [10] for x=0, 0.1 and 0.5, with similar lattice parameters (a=3.32 Å, b=10.99 Å and c=8.81 Å), as verified by electron diffraction, and energy dispersive X-ray (EDX).

b) $ZrCr_2$ and $ZrFe_2$ - Both of these alloys exhibited a mixture of bcc Fe or hcp Zr and the corresponding intermetallic phase. Diffraction patterns from both intermetallic phases were consistent with a C15 $MgCu_2$ Laves phase face-centered-cubic structure [11,12]. The compositional

analysis performed by EDX was consistent with the reported stoichiometry within the margin of error (±2%). Those alloys exhibited two different microstructures for the intermetallic compound. Figure 1 shows the general aspect of a $ZrCr_2$ alloy. In this alloy and in the corresponding $ZrFe_2$ alloy, the intermetallic was found both as a "bulk" phase (figure 1a), with large grains and a few stacking faults (B) or as part of an intimate mixture of the intermetallic compound (A) with a solid solution of zirconium in iron. The intermetallic phase designated "SF" in figure 2a, had a high density of stacking faults. This is also seen in $ZrFe_2$ (figure 2) (arrowed in the picture). Both bulk and "SF" phases had the C15 crystal structure.

c) h-($Zr_{1.5}Nb_{1.5}Fe$). By introducing Nb in the place of Zr, we formed a compound that had the approximate stoichiometry $Zr_{1.5}Nb_{1.5}Fe$ as verified by EDX. The sample also contained another compound of the type $(Zr,Nb)_2Fe$. The diffraction patterns from the $Zr_{1.5}Nb_{1.5}Fe$ phase could all be indexed assuming a hexagonal crystal structure with a=5.4 Å and c=8.8 Å. There are two possibilities reported in the literature for the identification of this phase. Woo, et.al. [13] have reported a $(Zr,Nb)_3Fe$ hcp phase with these lattice parameters, and Shishov, et.al. [43] have reported a $Zr(Nb,Fe)_2$ with a C14 structure. Although our stoichiometry is close to the first structure, the second structure C14 is a known Zr-Fe phase. At present we cannot distinguish between the two. Another study of Zr-Nb-Fe precipitates in Zircaloy also found a hexagonal structure with similar lattice parameters [14], although in that case the stoichiometry was different.

These compounds were examined before and after irradiation in a Philips CM-30 TEM at Chalk River Laboratory, a Philips 420 TEM at the Materials Characterization Laboratory at Penn State and a JEOL-100CX and Philips 420 TEM at the Center for Electron Microscopy at Argonne National Laboratory. Specific areas in the thin foils were identified for later irradiation and studied with diffraction and EDX. Electron irradiations at 0.9 MeV were conducted at the High Voltage Electron Microscope (HVEM) at the Center for Electron Microscopy at Argonne National Laboratory. The electron current can be measured with a Faraday cup, and calibrations have been performed to

determine the exact gaussian shape of the beam, as shown in figure 3. The HVEM has an ion beam attachment that allows for in-situ ion irradiation with a wide range of different ions and energies. These were used in the present study of irradiation-induced precipitation and dissolution in zirconium alloys.

Alloys a through c were irradiated with electrons until amorphous, at temperatures ranging from 25 to 250 K. Bright field and dark field micrographs were taken at regular intervals during the irradiation to record the progress of the transformation. The amorphization process was also followed by recording the change of the spot pattern in the diffraction pattern into a ring pattern.

The two zirconium alloys, Zr-20%Nb containing the ω-phase and the Zr-2.5%Nb were irradiated with 350 KV Ar ions and electrons at various temperatures ranging from 300 to 773 K to determine whether the ω-phase precipitates were destabilized or dissolved in the first case and whether the β-phase precipitated out of solution in the second case. The Ar ion energy was chosen so that the peak in the damage distribution as calculated by TRIM 92 occurred within the thin foil. Vacuum during these experiments was on the order of 10^{-7} torr. For the ω-phase samples the progress of the irradiation was followed by recording dark field pictures using a reflection from the ω-phase.

Results

Amorphization of Intermetallic Compounds

The amorphization process is shown in the bright field sequence in figure 4. This particular example refers to amorphization of Zr_3Fe at 180 K. As the dose is increased, first the higher-order bend contours are distorted (4b), then weaken and eventually disappear (4d). With continued irradiation, the lower-order bend contours disappear as well, while an amorphous ring is formed in diffraction. Finally, a dose is reached where using the smallest diffraction aperture it is possible to obtain an amorphous ring without any diffraction spots. This is defined as the dose for the onset of amorphization. In figure 4 it occurs around 630s. At the end of the amorphization process (which

was taken to 3600s without further changes in radius) the radius saturates at a value smaller than the beam radius as shown in figure 4f.

The growth of this amorphous zone is then tracked as a function of dose. Figure 5 shows the amorphous radius measured from the negatives as a function of irradiation time in $Zr_3(Fe_{0.9},Ni_{0.1})$ for several temperatures. It can be seen that the radius remains at zero until the transformation is achieved. At the onset of amorphization the amorphous radius increases abruptly and continues to increase with dose. The increase is abrupt at low temperature, showing that at low temperature there is no dose rate effect: for all dose rates the dose to amorphization is the same. This dose is defined as the critical dose. At higher temperatures the situation is different; as the dose rates decrease with increasing radii, the dose to amorphization increases, and the amorphous radius saturates at a radius smaller than the beam size. Thus at high temperature, the dose to amorphization increases with decreasing dose rate. In fact, there is a critical dose rate (corresponding to the saturation radius) at which the dose to amorphization goes to infinity. From the full kinetic information displayed in figure 6 it is possible to obtain the variation of the dose to amorphization with temperature as shown. Plotting the onset of amorphization against temperature we obtain the critical temperature for amorphization, shown in figure 6.

Critical Temperature for Amorphization

These data were obtained for all the compounds of interest. The results are shown in figure 6a and 6b. The curves are very reproducible, as we verified in repeating some of these experiments. As shown in the previous section, the exact temperature at which amorphization ceases is dependent on the dose rate. The critical temperatures reported here are for the peak dose rate but they do not vary much with the location of the cut in the kinetic curves (figure 5), as long as the cut is made within the first 30% of the radius.

There are several interesting features of the critical temperature which are described in the following and analyzed more thoroughly in the discussion section.

a) The lowest critical temperature is that of $ZrFe_2$, (around 80 K), followed by h-$Zr_{1.5}Nb_{1.5}Fe$ (~150K), $ZrCr_2$ (180 K) o-$Zr_3(Fe_{0.9}, Ni_{0.1})$, o-$Zr_3(Fe_{0.5}\ Ni_{0.5})$ o-Zr_3Fe (all at 220K) and Zr_2Fe (260 K).

It is interesting to note that $ZrCr_2$ and $ZrFe_2$ have the same crystalline structure, but a difference of 100 K in critical temperature. The critical dose for $ZrFe_2$ is also double that of $ZrCr_2$. Both of these results indicate that $ZrFe_2$ is more difficult to amorphize than $ZrCr_2$. In the $Zr(Fe_{1-x}, Cr_x)_2$ system the cubic phase C15 is stable for $x>0.9$ and $x<0.1$, while for $0.1<x<0.9$ the hexagonal C14 structure is stable [15]. Therefore, while it would be interesting to measure the dose to amorphization for intermediate x, the results would not be directly comparable to those for $x = 0$ and $x = 1$.

b) Another interesting feature is that the critical temperatures for $ZrCr_2$ and $ZrFe_2$ are different for the stacking faulted phase and the bulk phase (A and B in figure 2). It can be seen in figure 7 that for both $ZrCr_2$ and $ZrFe_2$ a higher stacking fault density increases the critical temperature by approximately 10 K. A higher density of stacking faults in $ZrFe_2$ reduces the critical dose by half. It should also be noted that the dose-to-amorphization vs. temperature for the stacking-faulted $ZrFe_2$ phase exhibits a "step" (two-fold increase) to a higher plateau at a temperature corresponding to the critical temperature for the low stacking fault density $ZrFe_2$ phase.

c) For the $Zr_3\ (Fe_{1-x}, Ni_x)$ system, the critical temperature is 220 K for $x = 0$, 0.1 and 0.5. The curves overlap for the full temperature range studied, within experimental error. There is thus, no effect of internal stoichiometry on the susceptibility to amorphization in this system. This result is somewhat unexpected since, while Zr_3Fe is the stable phase at low temperature, this is not true in the Zr-Ni system where a mixture of Zr and Zr_2Ni would be stable at that stoichiometry. There is, therefore, some value of x at which $Zr_3(Fe_x,Ni_{1-x})$ becomes unstable with respect to

$Zr_2(Fe_y,Ni_{1-y})$ + Zr, so one would expect that additions of Ni would affect phase stability. We saw no evidence of this change in stability under low temperature in this work.

d) By contrast, the introduction of Nb in a Zr-Nb-Fe alloy had a large effect on the critical temperature of amorphization. As x varies from 1 to 0.5 the critical temperature decreases from 220K to about 150K. Clearly a major difference in this case is that the crystalline structure has changed from orthorombic at x = 0 to hcp at x = 0.5. This means that the substitution of Nb for either Zr or Fe (depending on whether we take the crystal structure in [13] or in [43]) has a major effect on crystal stability. It is interesting to note that the Nb_3Fe phase is not stable with respect to a mixture of Nb and the NbFe compound [16].

The highest critical temperature obtained was that of Zr_2Fe, which was found to be about 260K. This phase, formed by phase separation during cooling from the melt is metastable at low temperature.

Stability of ω-phase during irradiation

An in-situ irradiation sequence of ω-phase with Ar ions is shown in figure 7. The microstructure obtained after the heat treatment utilized but before irradiation is shown in the first frame. Cuboidal ω-particles are seen within the β-phase matrix. The cuboidal phase has a lower Nb content than the matrix and has the crystal structure of ω-CrTi [17]. The dark-field sequence is obtained using a ω-phase reflection. As the irradiation progresses no ω-phase precipitates out in the matrix, except for the last frame, which we attribute to contamination. The post-irradiation examination of this same sample shows the ω-phase particles still intact, and little evidence of precipitation in the β-matrix (figure 8). It is not possible to say for sure that ω-phase precipitation has not occurred in the β-matrix, since irradiation causes the appearance of many defects such as dislocation loops which confuse the contrast. A further complication is oxide formation on the thin foil during irradiation. It is possible therefore that defects on the order of < 100 nm would not have been

detected. The results from extensive experiments conducted on the stability of the ω-phase under different irradiation conditions can be summarized simply as that there were no effects observed of the 350 KeV Ar ion irradiation in the temperature range 573-673K to 5.8 dpa and 400 KeV electrons at 623K to 5 dpa on the ω-phase.

The experimental results are shown in Table 1. The results obtained in this work directly contradict those obtained by Nuttall and Faulkner [18], especially the electron irradiation experiment, which was conducted under the same conditions. We did observe a loss of contrast akin to the mottled contrast reported in their paper (see figures 7 & 8), but ascribe it to surface contamination. Detailed post-irradiation analysis confirmed this last hypothesis: it was not possible to light up any of the "particles" that made up this contrast using the dark field reflections from the cuboidal ω-particles as seen in figure 8c. These results are in agreement with those of Hernandez and Potter [19], who did not observe any effect on the ω-phase after irradiation to 10.8 dpa with 3 MeV Ni ions at 425°C. We also observed the same oxide superlattice reflections in the $(100)_\beta$ diffraction pattern as observed in [19], indicating that even at 10^{-7} torr, there are sample contamination problems.

Precipitation of β-phase during irradiation

For Nb contents above 0.9 the bcc high temperature β-phase is stabilized at room temperature. Precipitation of the β-phase from solid solution in the α-matrix in Zr 2.5%Nb has been observed under neutron [3,20], proton [21], and electron [22] irradiation. In this work, we attempted to reproduce these results using in-situ Ar ion irradiation, and monitoring the possible appearance of the β-phase in the α-phase by setting up the correct dark field conditions from the bulk β-phase. Figure 9 shows a dark field for a β-phase stringer in Zr-1%Nb after irradiation to 2.5×10^{14} Ar ion/cm^2. No precipitation is visible in the matrix. The Zr-2.5%Nb samples were irradiated to a fluence of 10^{15} ion/cm^2 (2.33 dpa) at temperatures of 573, 673 and 733 K. The Zr 1%Nb sample was irradiated to 2.5×10^{15} ion/cm^2 (5.8 dpa) at 723 K. In both cases the matrix exhibited a high defect concentration at

the end, but no β-phase precipitation was observed. The contrast after 2.5 x 10^{15} ion/cm^2 is made more confused by the presence of oxide stringer and small dislocation loops (figure 10), which do not allow us to completely rule out that some fine precipitation may have taken place.

Discussion

Amorphization

Amorphization under irradiation occurs when the accumulation of damage caused by the incident particles makes it favorable for the material to exchange the defected long-range order of the irradiated crystal for the short-range order of the amorphization structure. Pure metals and metallic solid solutions are not susceptible to amorphization, because when irradiated, they can only store topological defects (point defects, dislocations), whereas intermetallic compounds can store anti-site defects (chemical disorder) in addition.

The ordered nature of the crystalline structure of intermetallic compounds originates from the imperative of maximizing the number of unlike atom pairs [23]. This is especially true for compounds which have a large negative heat of mixing such as those studied in this work. The root cause of amorphization is the need to maintain a high concentration of unlike pairs in the material even under irradiation. As point defects and anti-site defects are created by irradiation, the number of unlike pairs in the irradiated solid decreases until it becomes favorable for its atoms to rearrange themselves in an amorphous structure where the requirements of chemical bonding can be more closely met, even at the expense of destroying crystallinity.

In the amorphous material, the local environment or short-range order is very similar to that in the undefected crystalline material [24], indicating the material recovers the short-range order to compensate for the long-range order it loses as it amorphizes. Amorphization can be thus seen as a compromise between the need to minimize disruption to chemical and topological order and the kinetic demands imposed on the material by irradiation.

There are two aspects to the amorphization process. One is the accumulation of damage creating the necessary conditions for amorphization. The other is the actual rearrangement of atoms attendant upon the transformation. Taking the second point first, there is evidence that the transformation occurs fast compared to the total irradiation time [25], possibly by a catastrophic collapse induced by an elastic instability of the damaged structure [26]. That being the case, the rate-controlling step for irradiation-induced amorphization is the accumulation of enough damage in the structure.

The amorphization process depends then, on the relative rates of damage accumulation and annealing. The two processes occur in parallel under irradiation, their relative importance changing with temperature. At very low temperature, the point defects responsible for annealing are immobile, and damage accumulates as fast as it is produced. As the temperature increases, different defects become mobile. The annealing from the motion of these defects is proportional to the defect concentration and to their mobility, $\nu \exp(-E_j/kT)$ where E_j is the migration energy of defect j and ν the vibration frequency. The level of damage necessary for amorphization can be characterized by an increase in the free energy of the irradiated solid equal to the difference in free energy between the crystal and the amorphous [25], or by an increase in the mean-square displacement of the atoms in the defected crystal relative to the pristine one, as specified by the generalized Lindemann criterion [27]. However we estimate it, if the critical level of damage is L_{crit}, then:

$$L_{crit} = (\dot{G} - \dot{A})\, t_{irr}^{am} \qquad (1)$$

where $\dot{G}$ is the damage rate, $\dot{A}$ the annealing rate and t_{irr}^{am} the irradiation time to amorphization.

In this formulation, the critical temperature T_c is the temperature at which $\dot{G} = \dot{A}$ so that at T_c, t_{irr}^{am} is infinite.

$\dot{A}$ is given by

$$\dot{A} = C_1 \sum_j C_j \nu_j e^{-E_j/kT} \quad (2)$$

where C_1 is a constant, ν_i is the vibration frequency of defect; and C_j is the concentration of defect j. The damage rate $\dot{G}$ is given by

$$\dot{G} = \phi \sigma_d , \quad (3)$$

where Φ is the particle flux, and σ_d is the displacement cross-section.

Within this framework, we can understand the steps in the dose to amorphization as the temperatures at which a certain type of defect becomes mobile thereby increasing the annealing rate. If the increase is not enough to match damage production, it will still be possible to amorphize, but it will take longer, hence a "step" is observed. Equation 1 implies that the higher the rate of damage, the higher the temperature at which $\dot{A} = \dot{G}$, or the higher T_c in agreement with experiment [9,25]. The difference is not large, however: increasing the dose rate by a factor of six increases the critical temperature by approximately 20 K [9].

For a given dose rate, changing the damage mechanism changes the critical temperature for amorphization [5,28]. The biggest difference is between cascade-producing irradiation (ion and neutron) and electron irradiation. In the case of Zr_3Fe the difference between the T_c for electron and Ar ion irradiation is approximately 350 K [29]. This difference is similar to that observed in the critical temperature for amorphization of $Zr(Cr,Fe)_2$ precipitates in Zircaloy when induced by electrons (300 K) and neutrons or ions (650 K) [30].

This work also shows that the presence of stacking faults can change the critical temperature. This could be due to a change in point defect mobility or possibly to a change in diffusion modes caused by the presence of the stacking faults. Another possible explanation is that the stacking faults

increase the energy stored in the lattice, thereby decreasing the amount of damage necessary to amorphization.

The difference in the critical temperatures of $ZrCr_2$ and $ZrFe_2$ is, by contrast, likely to be caused by different migration energies of defects in the two structures. The higher dose-to-amorphization at low temperature for $ZrFe_2$ as compared to $ZrCr_2$ indicates that annealing mechanisms are much more efficient in $ZrFe_2$ than $ZrCr_2$.

We attribute the difference between the dose-to-amorphization of $ZrFe_2$ and $ZrFe_2$-SF at low temperature to a decrease in L_{crit} (equation 1) due to the presence of stacking faults rather than to a change in $(\dot{G} - \dot{A})$.

Previously published research on $Zr(Cr,Fe)_2$ precipitates in Zircaloy [5,25] showed the critical temperature to be around 300 K for 1.5 MeV electron irradiation. The discrepancy with T_c for $ZrCr_2$ is not great since in the previous study: 1) a beam heating correction of 20-40 K was included so the effective T_c was 260 K, 2) the dose rates were higher by a factor of three, and 3) the irradiation was taken to much higher values of dpa (up to three times as much). There is, however, a large difference between the T_c in $Zr(Cr,Fe)_2$ and $ZrFe_2$, suggesting that the migration energy of Fe is affected by the presence of Cr in $Zr(Cr,Fe)_2$. It is interesting to note that the T_c's for Zr_2Fe and Zr_2Ni [32] are very similar.

The steps found in the dose-to-amorphization vs. temperature curve for $ZrFe_2$ are of great interest. The presence of the steps in $ZrFe_2$ indicates that two types of defects become mobile, one at 60 K, one at 80 K. Similar steps have been previously seen in CuTi [33] and Zr_3Fe [34]. The interest lies in using the amorphization process to study the properties of defects in intermetallic compounds and comparing them to the properties of defects determined by molecular dynamics. This should enable us to discern which defects are responsible for annealing and what their dependence is on stoichiometry.

Irradiation Altered-Solubility

In a binary alloy, of a given overall composition, there is at each temperature a preferred combination of phases of set compositions which minimizes the overall free energy of the system. These are the equilibrium phases. The terminal solid solubility (TSS) in a given phase is the maximum amount of solute that can be held in solid solution within a primary phase. This solubility limit is a thermodynamic quantity and is only dependent on temperature. By establishing a limit for the amount of solute in solution, the TSS effectively controls the relative amounts of matrix and second phase formed.

When we try to apply these thermodynamic principles to commercial alloys in nuclear power reactors, we run into two types of difficulties which can alter phase equilibria: those related with the state of the material and those related with irradiation.

The state of the material can alter solubility in several ways. The TSS is measured for a well-annealed, binary alloy in equilibrium. All of these conditions are violated for commercial alloys. The addition of other alloying elements can change the apparent solubility of a given solute, for example by solute-impurity trapping. The presence of cold-work can also change the overall amount of solute contained in the matrix, for example, by decreasing the amount of solute in solution because of enhanced precipitation at dislocations. Finally the fabrication processes used in commercial alloys often do not produce equilibrium microstructures. For example, the β-quench process results in a finer distribution of second-phase precipitates and a higher alloying content in the matrix than in the α-recrystallized material.

Irradiation can also alter phase stability. Indeed, in a strict sense, it is not possible to speak of thermodynamically stable phases under irradiation, as several of the conditions necessary for thermodynamic equilibrium are not satisfied [35,36]. However, by describing the kinetics of the irradiation processes it is possible to discern the direction of variation of the material structure under irradiation. Irradiation can alter phase equilibria in two distinct ways: there can be irradiation

enhancement of phase transformations and irradiation inducement of phase transformations. Irradiation can thus either accelerate the appearance of the thermodynamically stable phase or induce the appearance of new phases not observed outside of irradiation.

β-phase Precipitation

It has been argued that the precipitation of β-phase within the α-phase of Zr 2.5%Nb should be classified as a radiation-enhanced transformation [22]. This is because their morphology is similar to that observed in β-quenched and aged Zr 2.5%Nb [43], and because post-irradiation annealing of neutron irradiated Zr 2.5%Nb either coarsened or left unchanged the precipitate distribution. If we accept the framework above, the precipitation of the β-phase in Zr 2.5%Nb is classified as a radiation-enhanced phase transformation. The fact that β-phase precipitation is observed under neutron, proton and electron irradiation indicates that no irradiation-specific process, such as cascade production, or specific secondary defect structures, are essential to the enhancement of that precipitation.

This precipitation is, therefore, likely to be controlled by diffusion of Nb atoms in α-Zr, and should be favored for high values of the typical diffusion length <x>, given by

$$\langle x \rangle = \sqrt{D_{Nb}\, t_{irr}} = \sqrt{C_j\, D_j\, t_{irr}} \qquad (4)$$

where D_{Nb} is the Nb diffusion coefficient, C_j is the defect responsible for Nb diffusion and D_j the defect diffusion coefficient. The calculation of defect concentrations under irradiation has been reviewed by Sizman [38]. Following his work, by determining the time to steady state in each of the above irradiations and the regime of operation (sink-dominated or recombination-dominated), we can estimate C_j. The time to steady-state τ is given by:

$$\tau = \frac{1}{\sum_k S_{kj} D_{sd}} = \frac{1}{\left(z_{sd}\rho_d + S_s\right) D_{sd}} \qquad (5)$$

where sd indicates the slowest defect, d stands for dislocation and s stands for surface. S_{kj} is the strength of sink k for the slowest defect, D_{sd} is the diffusion coefficient, z_{sd} is the bias factor, ρ_d the dislocation density and S_s the surface sink strength when spread over the bulk. For the parameters in table 2, τ is smaller than 1 s for all the irradiations considered, which means that steady state is established as soon as the dislocation structure is fully developed.

We define the parameter ε as:

$$\varepsilon = 1 + \left(\frac{S_s}{S_d}\right) = 1 + \frac{C_s}{C_d} = 1 + \frac{2a_o/h}{\rho_d a_o^2} = 1 + \frac{2}{\rho_d a_o h} \approx 660 \qquad (6)$$

where C_s and C_d are the surface and dislocation sink concentrations when spread over the material, h is the foil thickness and a_o the interplanar distance. The parameter ε is the ratio of the total sink strength to the dislocation sink strength. For the values in table 2, applicable to a foil thinned for TEM, with a dislocation density of 10^{10} cm^{-2}, $\varepsilon \approx 660$ which means that even when fully developed the dislocation sink is negligible compared to the surface sink. For a 1 mm thick disk as used in [20] or the 0.5 mm thick disks used in [21] and [22], ε is respectively 1.07 and 1.93. We can estimate the time to steady state and the regime of point defect behavior, (sink-dominated or recombination-dominated) using rate theory [37,38]. All the irradiations listed in table 3 were done in conditions corresponding to a sink-dominated regime and where a steady-state is quickly obtained. In that case, for a solid containing dislocation sinks and a surface sink,

$$\langle x \rangle = \sqrt{\frac{\dot{G}_{eff} D_j t_{irr}}{\sum_k S_{kj} D_j}} = (S_{dj})^{1/2} \left(\frac{\dot{G} f t_{irr}}{\varepsilon}\right)^{1/2} \qquad (7)$$

where S_{kj} is the strength of sink k for defect j and the subscript d stands for dislocation. We calculated the value of <x> from equation 7, using the parameters in table 2. The fraction of freely-migrating defects f produced by each type of irradiation is a matter of current research interest [42].

Because of intra-cascade recombination, the actual amount of defects that survive the cascade and are free for long-range migration, is much smaller than the number calculated from the Norgett-Robinson-Torrens formula $\nu_{NRT}(T) = 0.8\ T/2\ E_d$ [ASTM Standard E521-83]. Here $\nu_{NRT}(T)$ is the number of displacements caused by an atom energy T and E_d is the displacement energy. We use here the relative efficiency values proposed in [42], assuming 100% efficiency for electrons (f=1), 50% efficiency for protons (f = 0.5) and 5% efficiency (f = 0.05) for neutrons and heavy ions. The reason for the difference is the sharp decrease of f with increasing mean recoil energy. The results obtained are summarized in (Table 3), presented in the form of the ratio χ_i:

$$\chi_i = \frac{\langle x \rangle_i}{\langle x \rangle_n} = \frac{\left(\sqrt{Dt_{irr}}\right)_i}{\left(\sqrt{Dt_{irr}}\right)_n} = \left[\frac{\dot{G}_i\, f_i\, t^i_{irr}\, \varepsilon_n}{\dot{G}_n\, f_n\, t^n_{irr}\, \varepsilon_i}\right]^{1/2} \tag{8}$$

where $\langle x \rangle_i$ refers to irradiation i and $\langle x \rangle_n$ refers to neutron irradiation at 770 K. χ_i is 1 for neutron irradiation, slightly bigger than 1 for electron and proton irradiation, while for Ar ion irradiation it is about 10^{-2}. In this scenario, the appearance of the β-phase is correlated with a high χ_i. In heavy ion irradiation of thin foils, the presence of the free surface combined with the low f depresses the defect concentration below the level necessary to induce enough transport to cause β-precipitation. That is the likely reason for the absence of β-precipitation under Ar irradiation in this work.

It is questionable whether β-phase precipitation in the α-phase requires Nb transport from the β- to α-phase. If that were the case, the thin foil geometry would further reduce the possibility of precipitation. However, the fact that preferential β-precipitation near β-α grain boundaries was not observed argues for precipitation to occur using the Nb already in the α-phase.

The absence of β-precipitation near grain boundaries during bulk electron irradiation [22] can be qualitatively explained by the depression in the defect concentration caused by the proximity to the grain boundary defect sink. It would be interesting to investigate whether bulk heavy ion irradiation (at a lower dose rate) or thin foil electron irradiation could also produce β-precipitation. We should

note that for bulk Ar ion irradiation ε is much smaller due to the absence of the surface sink, and precipitation may occur. However, one effect not considered here, namely the spatial superposition of cascades along the ion track during Ar ion irradiation, could further reduce f and hamper precipitation.

ω-phase Dissolution

In this work, neither a direct attempt to reproduce ω-phase dissolution with electron irradiation, nor other attempts to cause it to occur with ion irradiation in this work and in [19] were successful. These results call into question the results obtained by Nuttall and Faulkner showing ω-phase dissolution and refinement under electron irradiation.

The dissolution of phases should, in general, be favored under ion irradiation relative to electron irradiation because the presence of cascades enables such processes as recoil resolution [39], interfacial mixing [40] and disordering and amorphization [41] which favor precipitate dissolution. In the present case, since the ω-phase has a lower Nb content than the β-phase, in order for the precipitates to dissolve, there would need to be some mixing of Nb and Zr atoms, which would be driven by the processes above. It is, therefore, unlikely that electron irradiation would destabilize precipitates while ion irradiation would not.

Conclusions

The amorphization of several Zr-based intermetallic compounds and the stability of specific alloys to precipitation and dissolution were studied using in-situ charged-particle irradiation. The use of in-situ irradiation is shown to be a useful means of obtaining kinetic data that can be used to extend our knowledge of material behavior in irradiation environments. The following points are emphasized:

1. The critical temperature for amorphization T_c in the compounds studied increases with the density of pre-existing stacking faults and with increasing dose rate. For $ZrFe_2$, the athermal dose is reduced by a factor of two when more stacking faults are present.

2. A marked compositional effect on T_c was noted in the $ZrCr_2$-$ZrFe_2$ with the same C15 crystal structure, where changing Fe for Cr increases T_c by 100 K, and increases the athermal dose by a factor of two.

3. The increase in the Nb concentration $Zr_{1.5}Nb_{1.5}Fe$ compared to either $ZrFe_2$ or Zr_2Fe changed T_c, while the addition of Ni to $Zr_3(Fe_{1-x}Ni_x)$ up to $x = 0.5$ had no effect on its amorphization behavior.

4. The above results can be rationalized with a kinetic model that predicts amorphization occurs when the accumulation of radiation damage opposed by thermal annealing reaches a critical limit.

5. No β-precipitation was observed during irradiation of Zr-2.5%Nb with Ar ions at several temperatures. The discrepancy with other experiments is rationalized based on a simple diffusion length model.

6. The ω-phase present in Zr-20%Nb was found to be stable under Ar ion and electron irradiation. The results agree with those in [19] and contradict those in [18]. An explanation for the discrepancy based on sample contamination is proposed.

Acknowledgements

The authors would like to thank D. Phillips and H. Plattner of Chalk River Laboratories, and Stan Ockers, Ed Ryan and Loren Funk of Argonne National Laboratory for their expert technical assistance. Joseph Faldowski is grateful for the support for his thesis research from a Lab-Grad Fellowship from the Division of Educational Programs at Argonne. The interest and support of the Candu Owners Group (COG) Working Party 32, is gratefully acknowledged.

References

1. A. Jostons, P.M. Kelly, R.G. Blake and K. Farrell, Proceedings of the 9th Symposium on the Effects of Radiation on Materials, ASTM-STP 633, (1979), 46-61.
2. M. Griffiths, Journal of Nuclear Materials, 159 (1988), 190.
3. C. Lemaignan and A.T. Motta, "Zirconium Alloys in Nuclear Applications", in Nuclear Materials, B.R.T. Frost, ed., vol. 10B, Material Science and Technology Series, R.W. Cahn, P. Haasen and E.J. Kramer, eds., 1-51.
4. A. Strasser, D. O'Boyle and R. Yang, International Topical Meeting on LWR Fuel Performance, West Palm Beach (1994) 3-14.
5. A.T. Motta, F. Lefebvre and C. Lemaignan, 9th International Symposium on Zr in the Nuclear Industry, ASTM-STP 1132 (1991), 718-739.
6. D. Charquet and E. Alheritière, Workshop on Second-Phase Particles in Zircaloys, Erlanger, Germany (1985).
7. A. Seibold and K.N. Woods, ibid [4], 633-642.
8. D. Gilbon and C. Simonot, 10th International Symposium on Zirconium in the Nuclear Industry, ASTM-STP 1245, A.M. Garde and E.R. Bradley eds., (1994), 521-548.
9. A.T. Motta, L.M. Howe and P.R. Okamoto, Journal of Nuclear Materials, 205 (1993), 258-266.
10. F. Aubertin, V. Gonser, S.J. Campbell, and H.G. Wagner, Z. Metallkd, 76 (1985) 237.
11. D. Arias and J.P. Abriata, Bull. Alloy Phase Diagrams, vol. 9 (5)(1988), 597.
12. D. Arias and J.P. Abriata, Bull. Alloy Phase Diagrams, vol. 7 (3)(1986), 237-243.
13. O.T. Woo and G.J.C. Carpenter, Proceedings of the 12th International Congress of Electron Microscopy, (1990), San Francisco Press, 132.

14. G.P. Sabol, R.J. Comstock, R.A. Weiner, P. Larouere and R.N. Stanutz, 10th International Symposium on Zr in Nuclear Industry, ASTM-STP 1245, A.M. Garde and E.R. Bradley, eds. (1994) 724-746.

15. D. Shaltiel, I. Jacob, D. Davidov, Journal of Less-Common Metals, 53 (1976), 117-131.

16. E. Paul and L.J. Swartzendruber, Bull. Alloy Phase Diagrams, vol. 7 (3)(1986) 248-254.

17. J.P. Abriata and J.C. Bolcich, Bull. Alloy Phase Diag. 3(1) (1982), 1711-1712.

18. K. Nuttall and D. Faulkner, Journal of Nuclear Materials, 67 (1977) 131-139.

19. O.G. Hernandez and D.I. Potter, in "Phase Stability Under Irradiation", AIME Symposium Proceedings, J.R. Holland, et al, eds., Metals Park, OH, 1980, pp. 601-612.

20. C.E. Coleman, R.W. Gilbert, G.J.C. Carpenter and G.C. Weatherly, in "Phase Stability Under Irradiation", AIME Symposium Proceedings, J.R. Holland, et al, eds., Metals Park, OH, 1980, 581-599.

21. C.D. Cann, C.B. So, R.C. Styles and C.E. Coleman, Journal of Nuclear Materials, 205 (1993) 267-272.

22. O.T. Woo, R.M. Hutcheon and C.E. Coleman, Materials Research Society Symposium Proceedings, vol. 373, I.M. Robertson, L.E. Rehn, S.J. Zinkle, W.J. Phythian, eds., (1995) 189-194.

23. J.H. Westbrook, ed., "Intermetallic Compounds", New York, Wiley, 1967, Chapter 1.

24. Ch. Hausleitner and J. Hafner, Journal of Non-Cryst. Solids, 144 (1992) 175-186.

25. A.T. Motta, D.R. Olander and A.J. Michaels, 14th International Symposium on The Effects of Radiation on Materials, ASTM-STP 1046, N.H. Packan, R.E. Stoller, and A.S. Kumar, eds., (1989), 457-469.

26. J. Koike, Phys. Rev. B, vol 47 (13)(1993) 7700-7704.

27. N.Q. Lam and P.R. Okamoto, Materials Research Society Bulletin 7 (1994), 41-46.

28. J. Koike, P.R. Okamoto, L.E. Rehn and M. Meshii, Metall. Trans. 21A, (1990) 1799.

29. L.M. Howe, D. Phillips, A.T. Motta and P.R. Okamoto, Surface and Coatings Technology, 66, (1994) 411-418.

30. A.T. Motta, L.M. Howe and P.R. Okamoto, MRS Symposium Proceedings, Vol. 279 (1993), M. Nastasi, L.R. Harriott, N. Herbots and R.S. Averback, eds., 517-522.

31. C.D. Cann, unpublished results.

32. G.B. Xu, M.Meshii, P.R. Okamoto and L.E. Rehn, Journal of Alloys and Compounds, 194(2) (1993) 401-405.

33. G.B. Xu, Proceedings of the 47th Electron Microscopy Society of America, (1989), 658.

34. L.M. Howe, D.P. McCooeye, M.H. Rainville, J.D. Bonnett and D. Phillips, Nuclear Inst. Methods in Physics Research, B59/60, (1991) 884.

35. H.J. Frost and K.C. Russell, in "Phase Transformations During Irradiation", F.V. Nolfi, ed., Appl. Science Pub., New York, 1983, 75-114.

36. G. Martin, Phys. Rev. B, vol. 30(3) (1984) 1424-1436.

37. H. Wiedersich, Radiation Effects, 12(1972), 111-125.

38. R. Sizmann, Journal of Nuclear Materials, 69 & 70 (1978), 386-412.

39. R.A. Nelson, J.A. Hudson, D.J. Mazey, Journal of Nuclear Materials 44 (1972) 318-330.

40. W.L. Johnson, Y.T. Cheng, M. Van Rossum and M-A. Nicolet, Nucl. Inst. and Meth. 67/8 (1985) 657.

41. A.T. Motta and C. Lemaignan, Journal of Nuclear Materials 195 (1992) 277-285.

42. L.E. Rehn and R.C. Birtcher, Journal of Nuclear Materials 205 (1993) 31-39.

43. V.N. Shishov, A.V. Nikulina, V.A. Markelov, M.M. Peregud, A.V. Kozlov, S.A. Averin, S.A. Kolbenkov, A.E. Novoselov, this symposium.

44. A.D. King, G.M. Hood and R.A. Holt, Journal of Nuclear Materials 185 (1991), 174-181.

45. Y. Etoh, K. Kikuchi, T. Yasuda, S. Koizumi and M. Oishi, International Topical Meeting on LWR Fuel Performance, Avignon, France (1991) 691-700.

46. V.F. Urbanic and R.W. Gilbert, in High Temperature Oxidation and Sulphidation Processes, J.D. Embury ed., Pergamon Press (1990) 182.

List of Figures

Figure 1. General aspect of $ZrCr_2$ alloy showing the difference between the two types of intermetallic compounds formed. (a) The region marked "A" consisted of a mixture of Zr and $ZrCr_2$-SF (with a high stacking fault density). The general aspect is shown in (b) where a phase marked "B" is shown which is also $ZrCr_2$ but with less stacking faults, while (c) shows a higher magnification picture of region B, showing a 2-b condition.

Figure 2. BF of $ZrFe_2$ alloy showing the two types of C15 $ZrFe_2$, a bulk phase designated $ZrFe_2$ and a high stacking fault density phase designated $ZrFe_2$-SF. Arrows indicate stacking faults.

Figure 3. Gaussian shape of the electron beam as measured by the Faraday cup. The precise determination of dose allowed the study of dose rate effects.

Figure 4. Amorphization of Zr_3Fe under electron irradiation at 180 K. Only a slight discoloration is present after 30s irradiation (a). After 210s (b) some higher order contours disappear and others become thinner and distorted. At 630s (d) there is the onset of amorphization. The amorphous radius increases until it saturates at 3000s at a value smaller than the beam size, shown approximately by the dotted line. The experiment was taken to 3600s with no change in the size of the amorphous region.

Figure 5. Dimensionless amorphous radius versus dose [electron/cm^2] for electron irradiation of $Zr_3(Fe_{0.9}, Ni_{0.1})$.

Figure 6. Dose to onset of amorphization under electron irradiation for (a) the $ZrFe_2$ - $ZrCr_2$ system and (b) o-$Zr_3(Fe_{1-x}, Ni_{1-x})$, h-$Zr_{1.5}Nb_{1.5}Fe$, Zr_2Fe.

Figure 7. In-situ sequence for Ar ion irradiation of ω-phase in Zr-20%Nb at 673K. We use a ω-phase reflection for the dark field to check for ω-phase precipitation in the β-matrix.

Figure 8. Dark field micrograph of ω-particles in Zr-20%Nb after irradiation to a fluence of 2.5×10^{15} Ar ion/cm^2 showing no breakup.

Figure 9. Dark field micrographs of β-phase filament (already present in the unirradiated material) in α-matrix in Zr-1%Nb, after irradiation to 2.5 x 10^{14} ion cm^{-2}. No additional β-precipitation is seen in the α-matrix.

Figure 10. Bright-field micrograph of the fine scale-damage (oxide stringers, oxide particles, small dislocation loops) in Zr-1%Nb after in-situ irradiation to 2.5 x 10^{15} Ar ion cm^{-2}. It is difficult to rule out precipitation on a scale finer than 100 Å.

Table 1 -- Irradiations of ω-phase in Zr-Nb alloys

Alloy	Particle	T(K)	Dose (dpa)	Result	Reference
Zr 12%Nb	1 MeV electrons	623	1-8	disintegration and reprecipitation	[18]
Zr 12%Nb	3 MeV Ni	698	10.8	no major change	[19]
Zr 20%Nb	350 KeV Ar	573	3	no major change	this work
Zr 20%Nb	350 KeV Ar	673	5.8	no major change	this work
Zr 20%Nb	900 KeV electrons	623	~5	no major change	this work

Table 2 -- Parameters for calculations

ρ_d - dislocation density - 10^{10} cm^{-2}

h - foil thickness - (cm):

bulk electron irradiation and proton irradiation - 5×10^{-2}
neutron irradiation - 0.1
Ar ion irradiation - 1×10^{-5}

a_o - interplanar distance - 3 Å

z_j - bias factor for defect j - 1

Table 3 -- β-precipitation in Zr-Nb α-phase

Alloy	Particle	Dose (dpa)	$\dot{G}$ (dpa/s)	T_{irr} (K)	t (s)	f (%)	ε	χ	Precipitate Size (nm)	Ref.
Zr 2.5%Nb	Neutron	0.62	1.28×10^{-7}	770	4.86×10^{6}	5	1	1	400	[20]
Zr 2.5%Nb	Neutron	0.74	1.52×10^{-7}	670	4.86×10^{6}	5	1	1.09	30	[20]
Zr 2.5%Nb	Neutron	0.8	1.65×10^{-7}	570	4.86×10^{6}	5	1	1.13	not visible	[20]
Zr 2.5%Nb PT	Neutron	5.4	1.88×10^{-7}	570	2.88×10^{7}	5	1	3.05	< 10	[1]
Zr 2.5%Nb	3.6 MeV Protons	0.94	9.9×10^{-7}	720	9.52×10^{5}	50	1	3.78	5-30	[21]
Zr 2.5%Nb	10 MeV Electrons	1.2	8.17×10^{-7}	710	1.22×10^{6}	100	1	6.04	70	[22]
Zr 2.5%Nb	10 MeV Electrons	0.6	4.5×10^{-7}	713	1.33×10^{6}	100	2.3	4.27	30	[22]
Zr 2.5%Nb	10 MeV Electrons	0.6	4.5×10^{-7}	733	1.33×10^{6}	100	2.3	4.27	15	[22]
Zr 2.5%Nb	350 KeV Ar	2.3	1.27×10^{-3}	573	1.83×10^{3}	5	660	7.7×10^{-2}	no precipitation bigger than 10 nm	this work
Zr 2.5%Nb	350 KeV Ar	2.3	3.35×10^{-3}	673	6.95×10^{2}	5	660	7.7×10^{-2}		this work
Zr 2.5%Nb	350 KeV Ar	2.3	3.67×10^{-3}	773	6.33×10^{2}	5	660	7.7×10^{-2}		this work
Zr 1%Nb	350 KeV Ar	5.8	1.53×10^{-3}	723	3.8×10^{3}	5	660	1.22×10^{-1}		this work
Zr 2.5%Nb	3.6 MeV H_1,H_2,H_3	N/A	N/A	720	N/A	50	1.3	N/A	15-40	[31]

Terminology

t_{irr}^{am} - irradiation time to amorphization [s]

L_{crit} - critical level of damage for amorphization in dpa

$\dot{G}$ - defect production rate [dpa/s]

$\dot{A}$ - annealing rate [annealed defects per atom/s]

T_c - critical temperature for amorphization [K]

C_1 - proportionality constant

C_j - concentration of defect j [atom fraction]

ν_j - vibrational frequency of defect j [s^{-1}]

E_j - migration energy of defect j [eV]

Φ - flux of damaging particles [particle/s cm^2]

σ_d - displacement cross section [barn]

<x> - diffusion length [cm]

D_{Nb} - Nb diffusion coefficient [cm^2/s]

t_{irr} - irradiation time

D_j - diffusion coefficient of defect j [cm^2/s]

τ - time to steady state [s]

S_{kj} - sink strength of sink k for defect j [cm^{-2}]

D_{sd} - diffusion coefficient for slowest defect [cm^2/s]

S_s - surface sink strength [cm^{-2}]

z_{sd} - dislocation bias factor for slowest defect

ρ_d - dislocation density [cm^{-2}]

h - foil thickness [cm]

a_o - interplanar distance [cm]

ε - ratio of total sink strength to the dislocation sink strength

C_s, C_d - sink densities expressed in atom fraction.

f - fraction of freely-migrating defects

$\dot{G}_{eff}$ - effective defect generation rate [dpa/s]

$\nu_{NRT}(T)$ - number of displacements caused by ion energy T

E_d - displacement energy [eV]

k_B - Boltzman's constant [eV/k]

χ_i - ratio of Nb diffusion length under irradiation type i to that under neutron irradiation

t_{irr}^{i} - irradiation time under irradiation type i

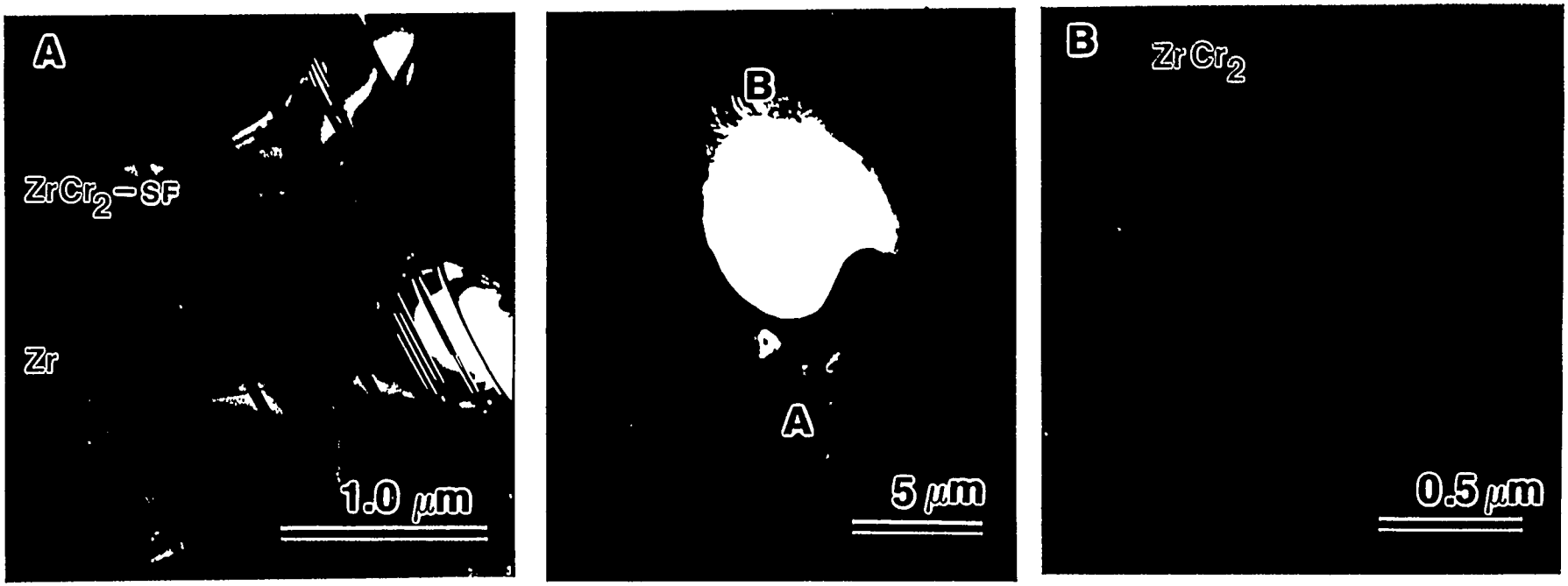

FIGURE 1 : MOTTA, FALDOWSKI, HOWE, OKAMOTO

FIGURE 2 : MOTTA, FALDOWSKI, HOWE, OKAMOTO

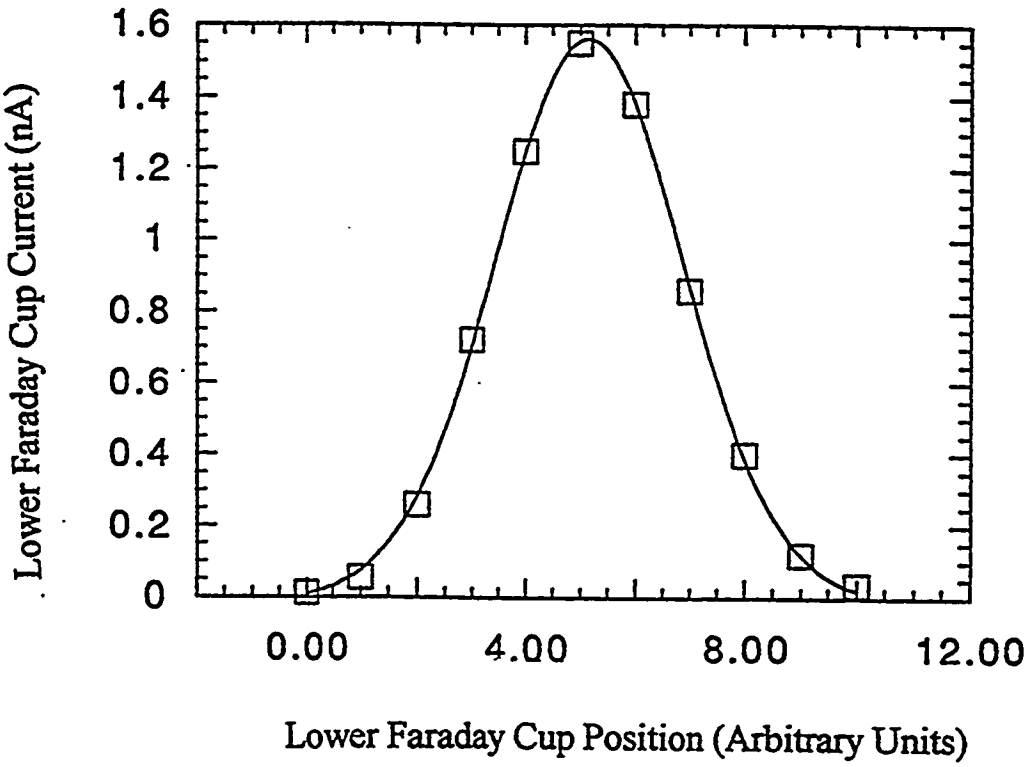

Figure 3 : MOTTA, FALDOWSKI, HOWE and OKAMOTO

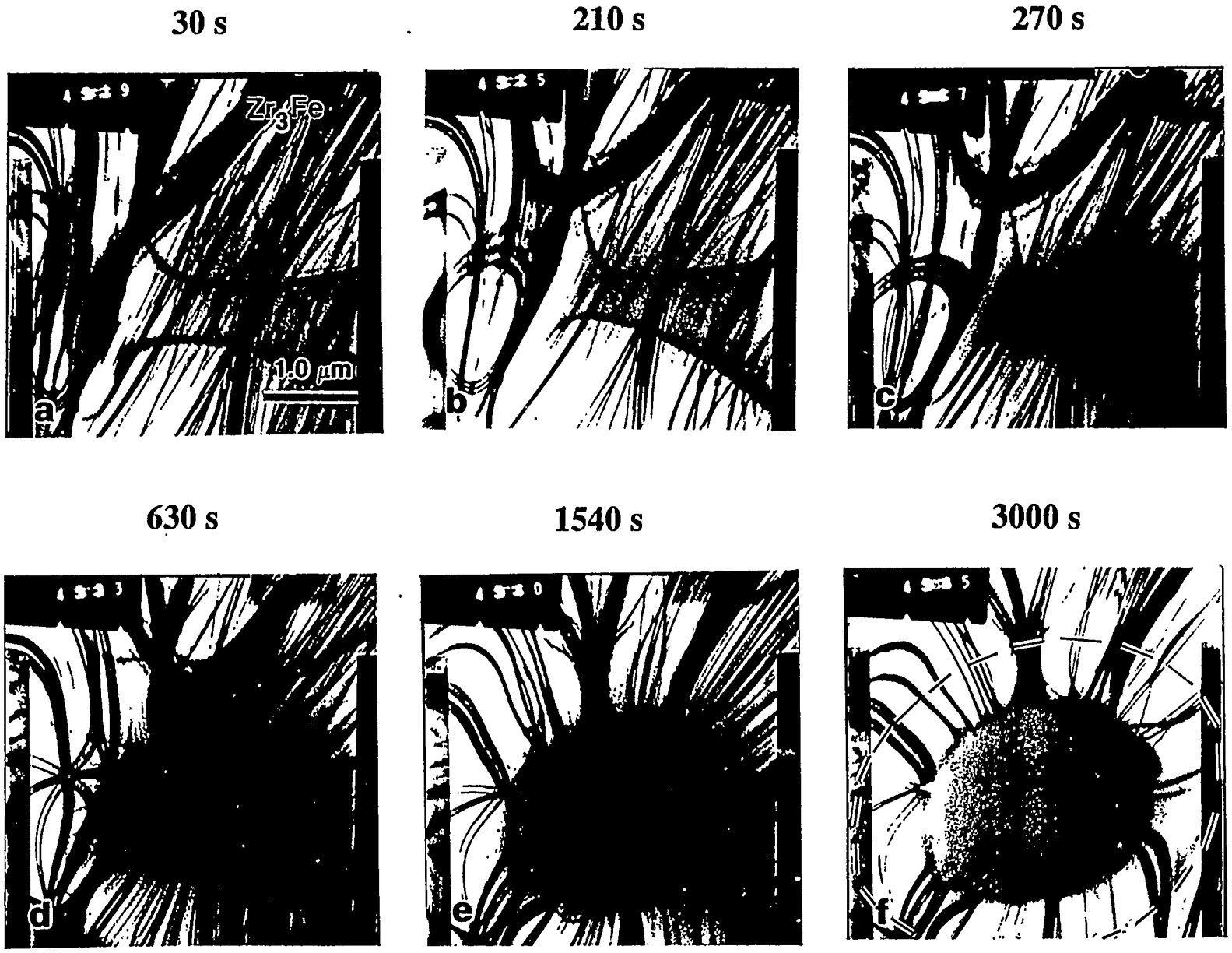

FIGURE 4: MOTTA, FALDOWSKI, HOWE, OKAMOTO

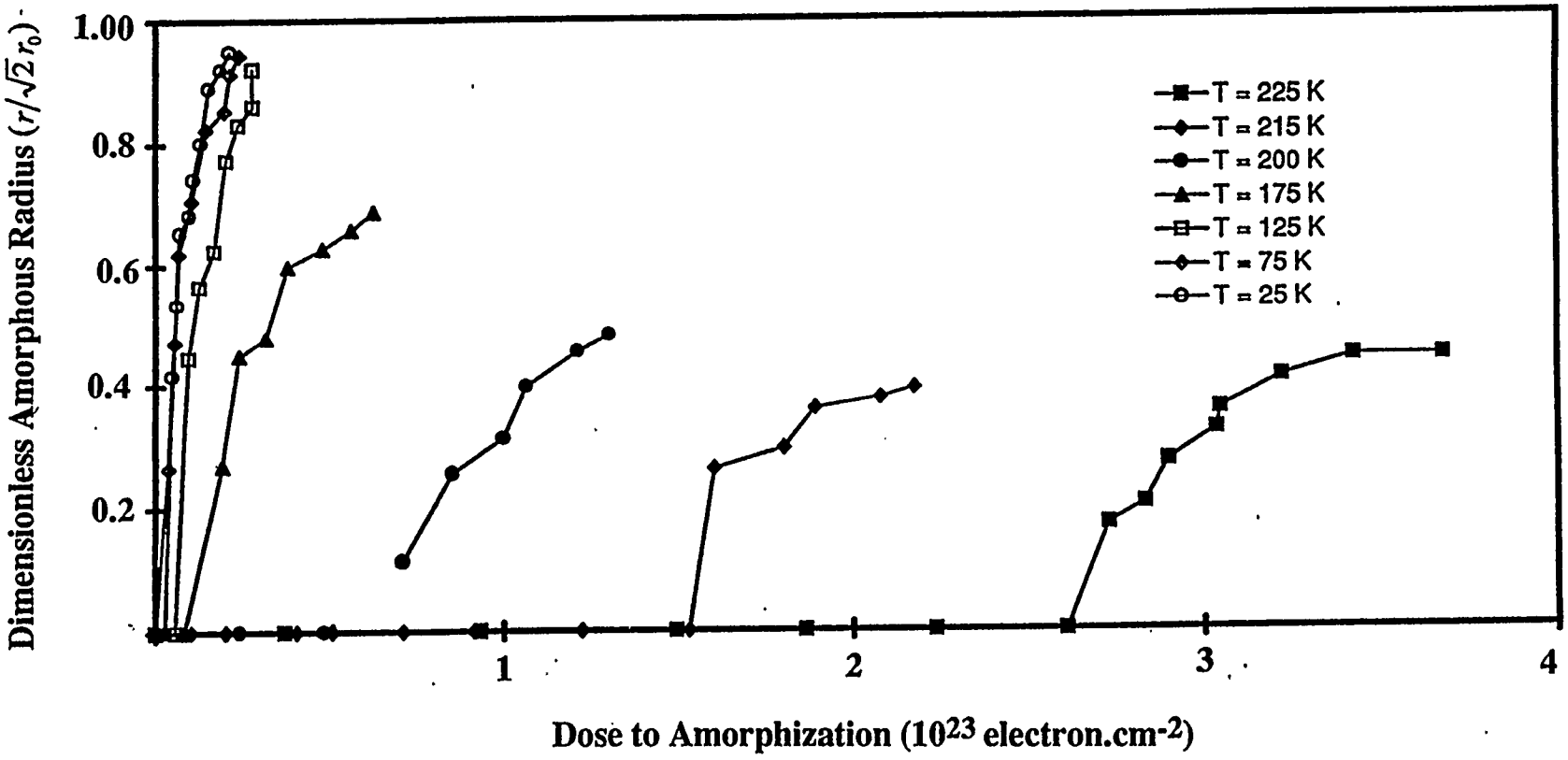

Figure 5, Motta, Faldowski, Howe, Okamoto

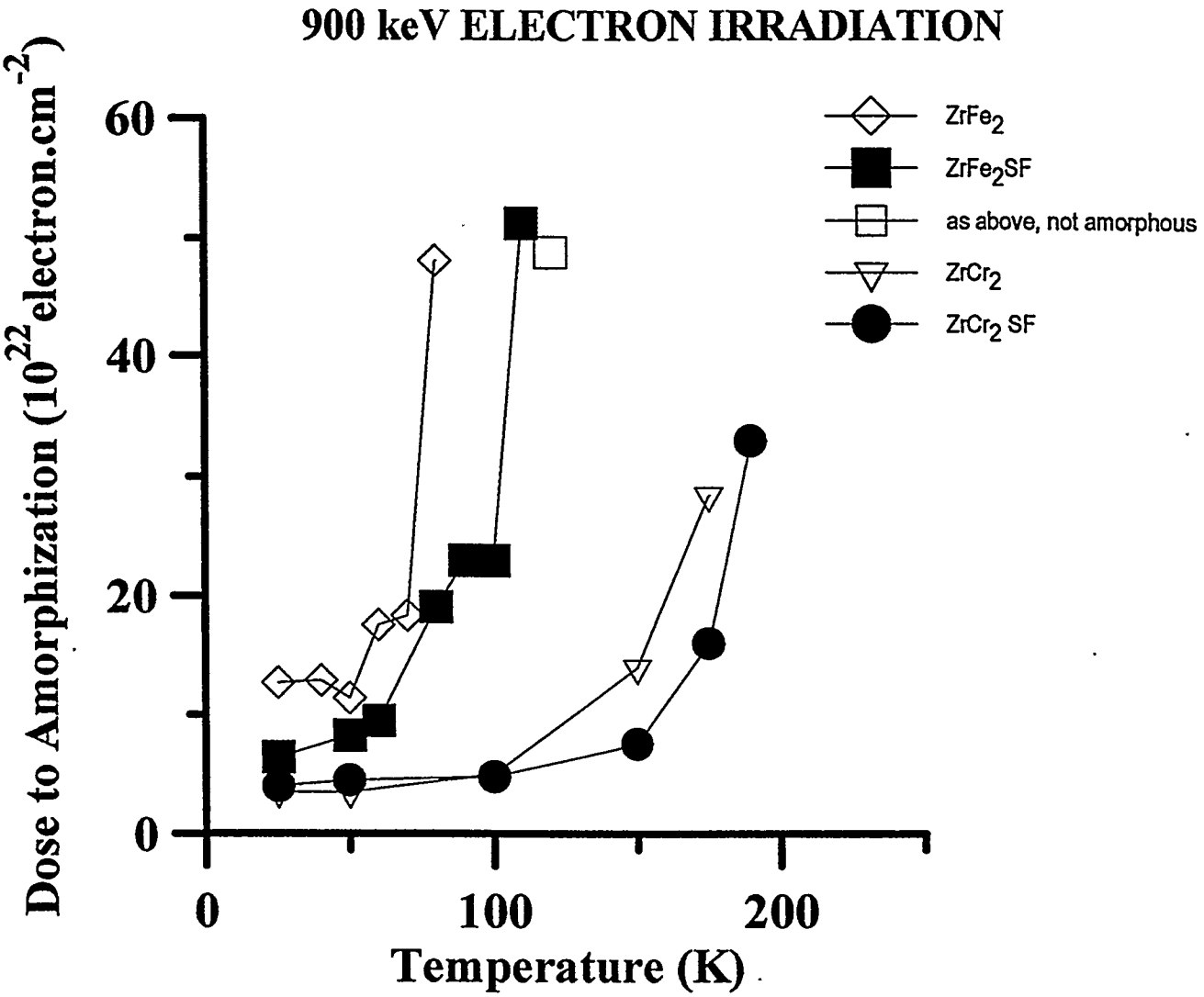

FIGURE 6 (a) Motta, Faldowski, Howe and Okamoto

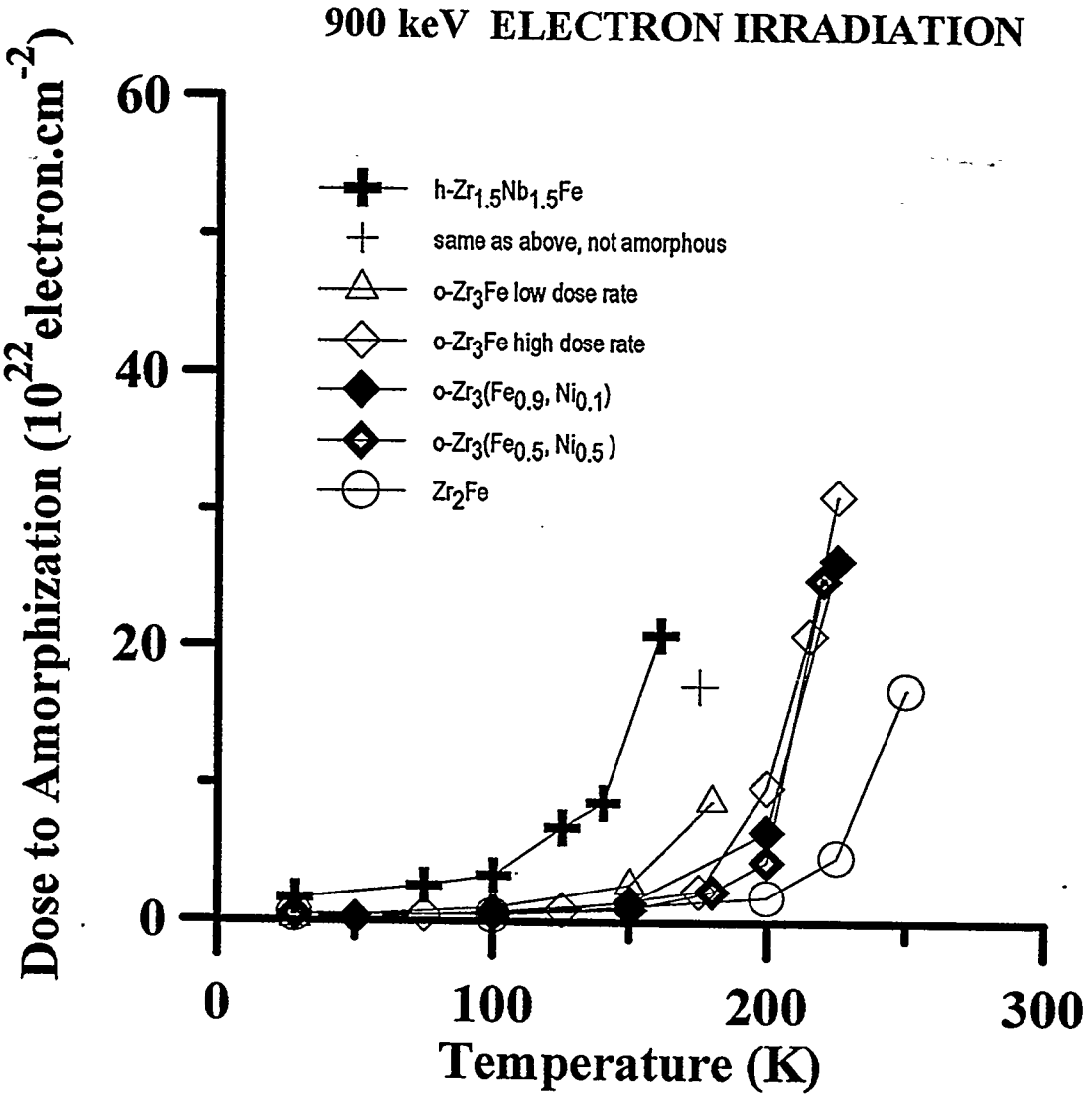

Figure 6 (b) Motta, Faldowski, Howe and Okamoto

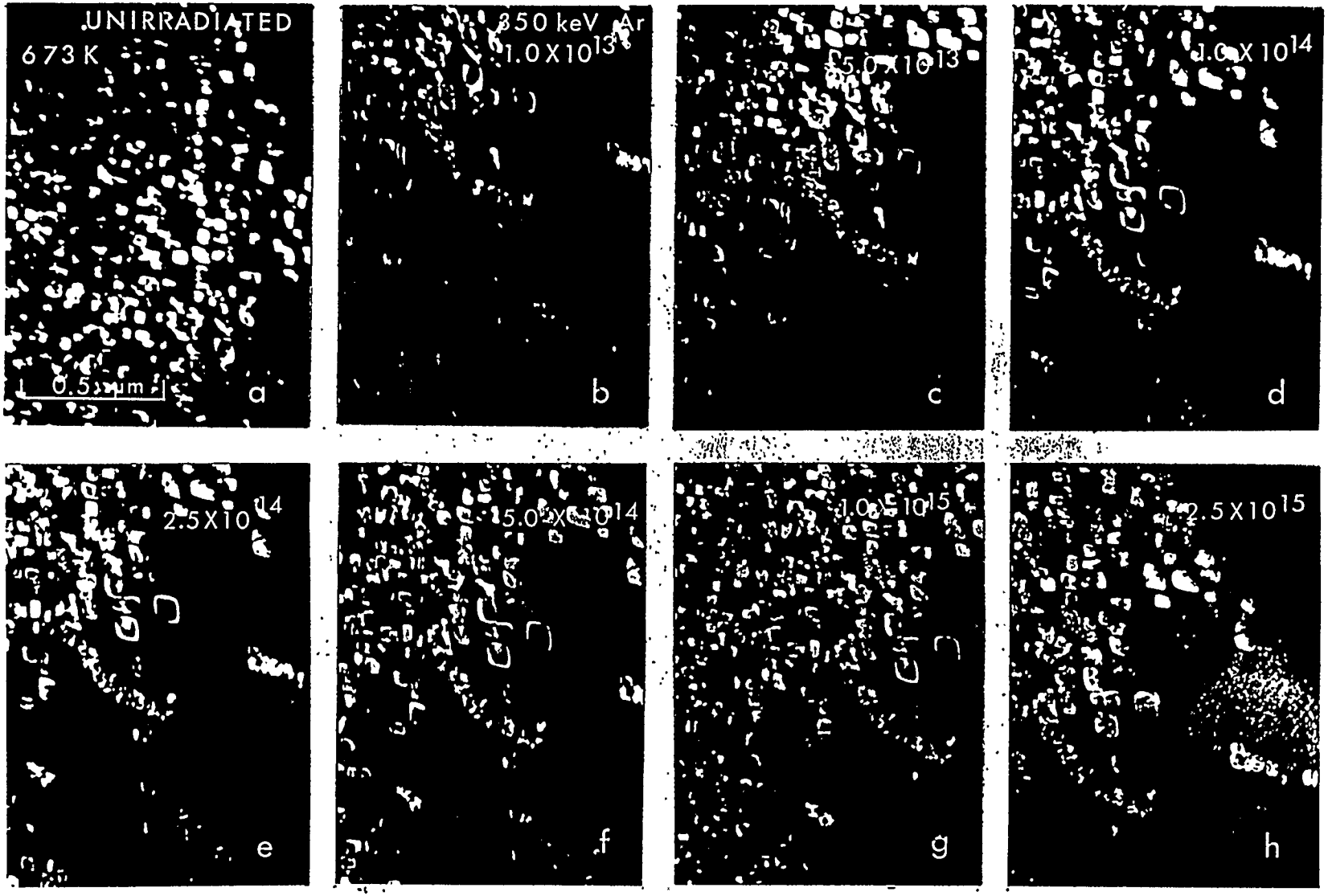

FIGURE 7 : MOTTA, FALDOWSKI, HOWE, OKAMOTO

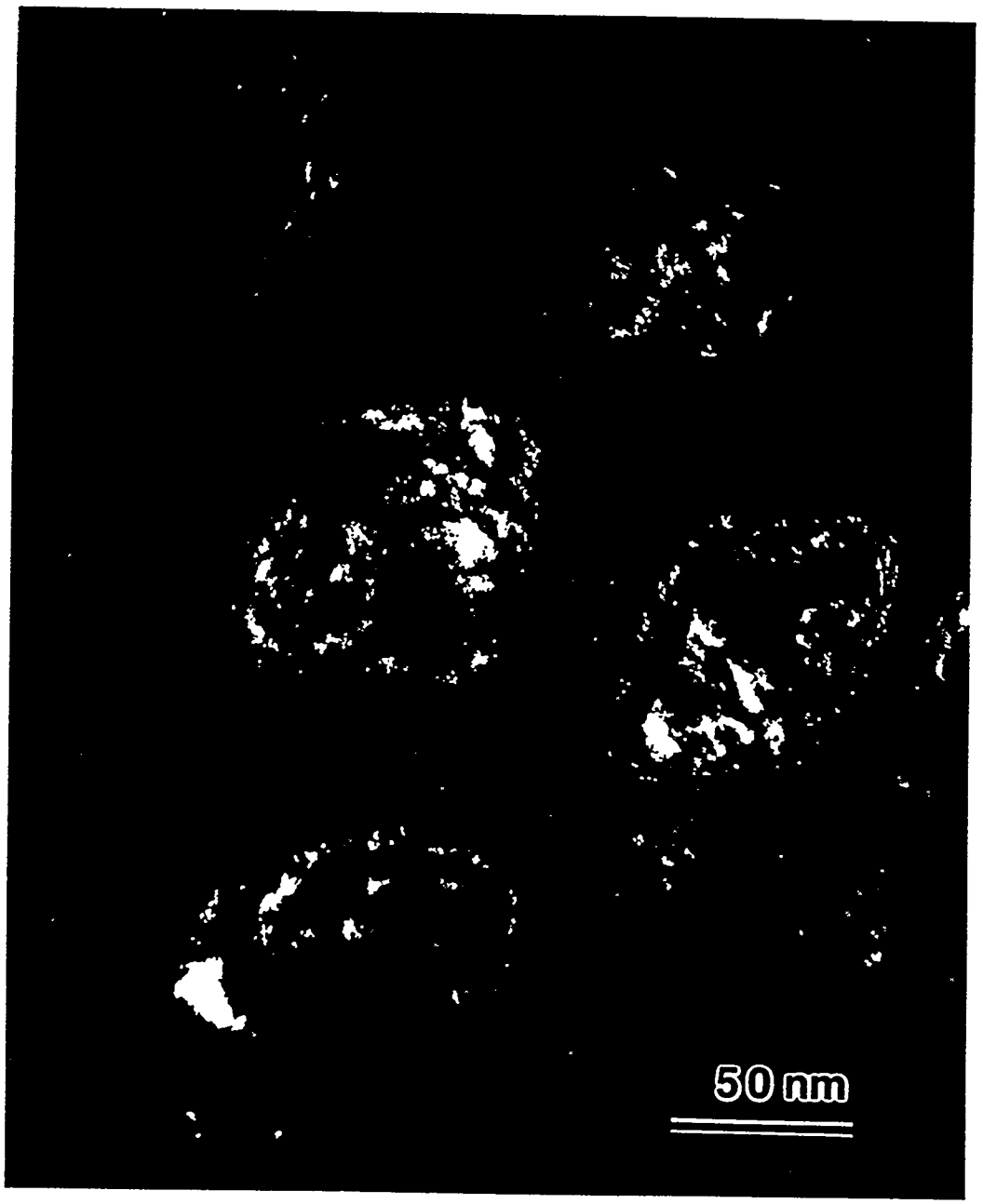

FIGURE 8: MOTTA, FALDOWSKI, HOWE, OKAMOTO

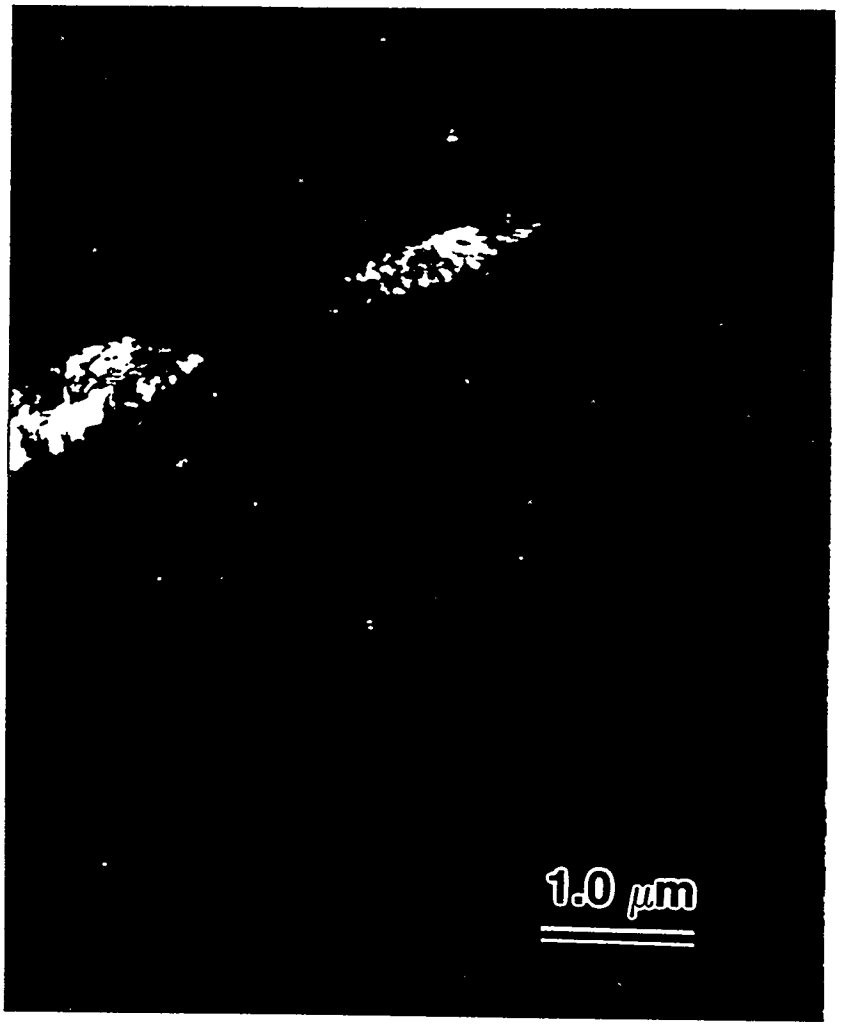

FIGURE 9 MOTTA, FALKOWSKI, HOWE, OKAMOTO

FIGURE 10: MOTTA, FALDOWSKI, HOWE, OKAMOTO